Journal of Materials Chemistry A

COMMUNICATION

View Article Online
View Journal | View Issue

Cite this: J. Mater. Chem. A, 2024, 12, 3258

Received 29th October 2023
Accepted 12th January 2024

DOI: 10.1039/d3ta06595b

rsc.li/materials-a

Atomistic picture of electronic metal support interaction and the role of water†

Lukáš Fusek, [ab] Matteo Farnesi Camellone, ‡[c] Michal Ronovský, §[b] Maximilian Kastenmeier, [a] Tomáš Skála, [b] Pankaj Kumar Samal, [b] Nataliya Tsud, [b] Sascha Mehl, [d] Jan Škvára, [b] Tomáš Dolák, [b] Vitalii Uvarov, [b] Martin Setvín, [b] Viktor Johánek, [b] Stefano Fabris, [c] Olaf Brummel, [a] Jörg Libuda, [a] Josef Mysliveček, *[b] Simone Piccinin *[c] and Yaroslava Lykhach *[a]

Single atom catalysis (SAC) represents an emerging area of heterogeneous catalysis but faces challenges related to the low density of active sites and poor thermal stability. In this work, we present new fundamental insights into the nature of electronic metal support interactions (EMSI) coupled with cation exchange, which yield high density of atomically dispersed noble metals on defect-free terraces of cation-terminated reducible oxides. On well-ordered Co_3O_4(111) films, the mechanism involves temperature-controlled substitution of surface Co^{2+} and sub-surface Co^{3+} cations by Pt^{2+} and Pt^{4+} species, respectively. The cation exchange with Co^{2+} is coupled with the partial reduction of Co_3O_4(111), while the cation exchange with Co^{3+} involves the charge disproportionation within the Pt species. In the presence of co-adsorbed water, the Pt^{4+} species are stabilized at the surface in the form of triaqua complexes.

Electronic metal support interactions (EMSIs) are ubiquitous in heterogeneous catalysis.[1–5] The phenomenon is associated with the charge transfer at the metal/oxide interface resulting in a partial oxidation of the noble metal deposit and a partial reduction of the support.[5–7] The magnitude of the charge transfer strongly depends on the size of the noble metal nanoparticles and the structure of the support.[7] In the regime of low metal loadings, noble metals can be stabilized in the form of cations which serve as active catalytic sites in single-atom catalysts (SAC).[8–19] The concept of SAC gained significant attention due to ultimate noble metal utilization which allowed for remarkable reduction of costs.[8–12] However, SAC faces significant challenges associated with low-dispersion of noble metal and poor stability.[19–22] Both factors are controlled by the availability of the specific anchoring sites and the coordination environment of the noble metal cations. In particular, the atomic dispersion of noble metals on the energetically most favorable, oxygen-terminated oxide surfaces is controlled by defects.[23,24] For instance, on the most studied cerium oxide supports, the stabilization of the noble metals in the form of cations requires the presence of specific sites formed by nanostructuring.[25–27] However, nanostructuring of the reducible oxides does not provide sufficient densities of defects to achieve a high coverage of atomically dispersed noble metals in SAC. Therefore, current research focuses on new strategies to fabricate SACs with a high density of single-atom sites, ideally on defect-free supports.[28–36] The most successful approaches employ the EMSI associated with cation substitution on the cation-terminated surfaces of reducible oxides.[37–40] In this respect, significant insights have been obtained on model systems involving *e.g.* TiO_2, Fe_2O_3, Fe_3O_4, Co_3O_4 substrates.[13,37] On these surfaces, noble metal atoms exchange places with the surface cations assuming their coordination environment.[13] In some cases, the presence of water or hydroxyl groups has been found to promote the dispersion.[41,42] However, the complete mechanism of the EMSI, specifically the aspect of the charge transfer between the noble metal atoms and the reducible oxide during the cationic exchange and the role of water, has never been revealed. This is mostly because the evaluation of the charge transfer requires the quantification of the oxidation states of the reducible oxides (*e.g.* Ce^{3+}/Ce^{4+} ratio in CeO_2).[7] This task, however, is often challenging due to the complex shape of the transition metals core levels.[43–45]

Here, we combined scanning tunnelling spectroscopy (STM), synchrotron radiation photoelectron spectroscopy (SRPES), and density functional theory (DFT) to draw a comprehensive picture of the EMSI in the Pt/Co_3O_4(111)/Ir(100) model system.

[a]Interface Research and Catalysis, ECRC, Friedrich-Alexander-Universität Erlangen-Nürnberg, Egerlandstrasse 3, Erlangen 91058, Germany. E-mail: yaroslava.lykhach@fau.de

[b]Charles University, Faculty of Mathematics and Physics, Department of Surface and Plasma Science, V Holešovičkách 2, Prague 18000, Czech Republic. E-mail: josef.myslivecek@mff.cuni.cz

[c]Istituto Officina dei Materiali, Consiglio Nazionale delle Ricerche (CNR-IOM), Via Bonomea 265, Trieste 34136, Italy. E-mail: piccinin@iom.cnr.it

[d]Elettra-Sincrotrone Trieste SCpA, Strada Statale 14, km 163.5, Basovizza-Trieste 34149, Italy

† Electronic supplementary information (ESI) available: Experimental details, STM evaluation, DFT computation, IV-LEED analysis, full set of SRPES data, TPD. See DOI: https://doi.org/10.1039/d3ta06595b

‡ This author contributed equally and should be also considered as first author.

§ Present address: European Synchrotron Radiation Facility, 38043 Grenoble, France.

For the first time, the EMSI associated with the cation exchange is characterized with respect to both the structure of the Pt sites and the charge transfer between the Pt atoms and the $Co_3O_4(111)$ substrate. Our findings provide unprecedented atomistic insights into the details of the charge transfer during the cation exchange at the surface and sub-surface regions which can be employed for the rational design of SAC with high density of atomically dispersed noble metal species.

Our study is based on the use of well-ordered $Co_3O_4(111)$ films prepared by means of physical vapor deposition onto the Ir(100) in a multistep procedure[46] schematically shown in Fig. 1a (see ESI for details, Section S1†). The resulting structure is a normal spinel with Co^{3+} and Co^{2+} cations in octahedral and tetrahedral coordination, respectively. In the near-surface region, Co^{2+} and Co^{3+} cations occupy the first and the second cationic layers, respectively (Fig. 1a). Deposition of Pt onto the $Co_3O_4(111)$ support in ultrahigh vacuum yields Pt species which give rise to two Pt 4f photoemission doublets at 72.3 eV (Pt $4f_{7/2}$) and 74.0 eV (Pt $4f_{7/2}$) (Fig. 1b–d). Based on the binding energy, the peak at 72.3 eV (Pt $4f_{7/2}$) can be attributed to both atomically dispersed Pt^{2+} species and ultra-small $Pt^{\delta+}$ aggregates.[47,48] Note that the binding energy of supported metallic clusters is a function of their size.[49,50] As a result, the spectral contribution from small $Pt^{\delta+}$ aggregates is shifted by as much as 1.0 eV reaching a binding energy of 72.0–72.3 eV.[47] In contrast, the peak at 74.0 eV (Pt $4f_{7/2}$) can be exclusively assigned to Pt^{4+} species.[48]

Scanning tunneling microscopy (STM) revealed very characteristic structural changes when Pt was deposited on the $Co_3O_4(111)$ surface (Fig. 1e–h). Prior to Pt deposition, we observe well-ordered $Co_3O_4(111)$ terraces terminated by Co^{2+} cations in agreement with literature.[46] On the clean surface, we observed two types of specific structural features which appear as bright protrusions (circled yellow, species I) and dark depressions (circled cyan, species II) in Fig. 1e. After Pt deposition at 300 K in UHV, the species I disappears and the density of species II increases. In addition, we observe several new features. Among these, we identify the bright protrusions in registry with $Co_3O_4(111)$ (circled green, species III) and larger bright protrusions of a triangular shape located at threefold hollow sites (FCC sites) (circled red, species IV). At Pt coverages of 0.04 and 0.13 monolayers (ML), we found greater bright features that represent ultra-small $Pt^{\delta+}$ aggregates (circled orange) consisting of 2–3 and 5–6 atoms on average, respectively, in agreement with our earlier study.[47] The complete assignment of all surface species observed in Fig. 1f and g is provided in ESI (Fig. S1, Tables S1 and S2).† A more detailed analysis of the structural parameters of the species II–IV with respect to the surface Co^{2+} cations is given in ESI (Section S2).† Most importantly, the corresponding analysis verified atomic dispersion of the species III and IV (Section S2 and Table S2†) in Fig. 1f and g.

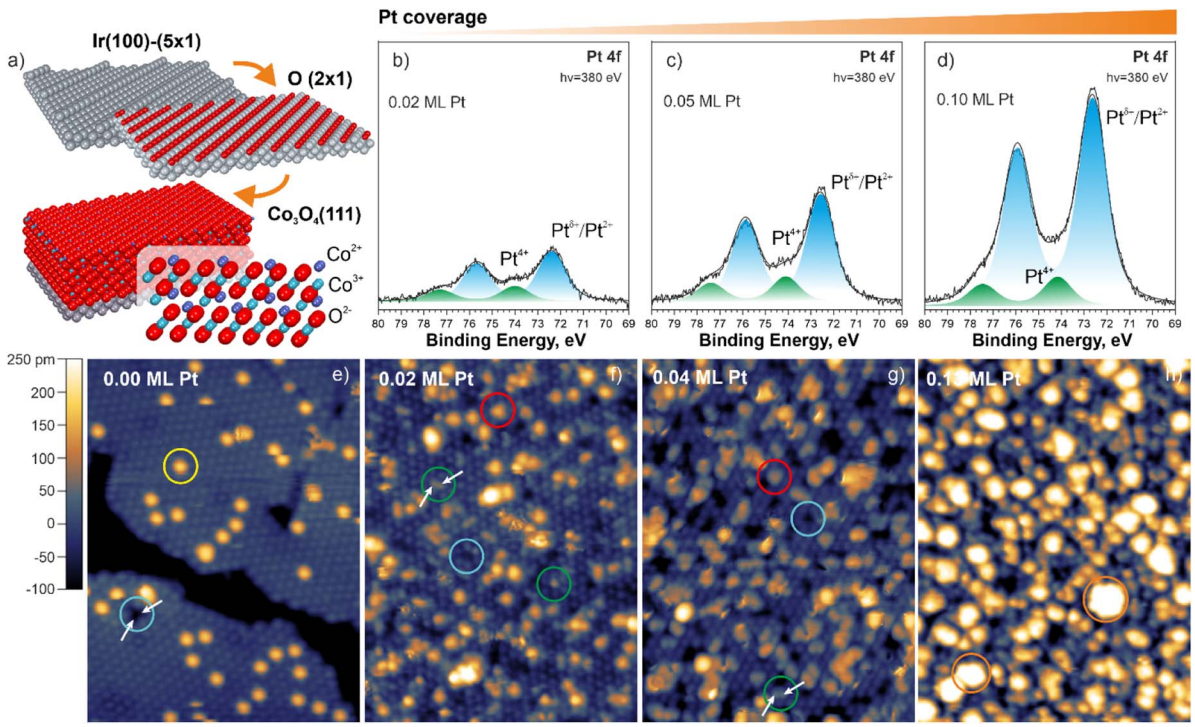

Fig. 1 Electronic and geometric structure of atomically dispersed Pt species and aggregates on $Co_3O_4(111)$: preparation of well-ordered $Co_3O_4(111)$ film on Ir(100) (a); Pt 4f spectra (b–d) and STM images obtained from $Co_3O_4(111)$ (e) and Pt/$Co_3O_4(111)$ model systems (f–h) as a function of Pt coverage. The representative features assigned to atomically dispersed species I–IV are circled yellow (species I), cyan (species II), green (species III), and red (species IV). The features that represent ultra-small $Pt^{\delta+}$ aggregates are circled orange. The species of the same type in the close proximity to each other are labelled by white arrows. STM images obtained with tip bias and tunnelling current of −2.0 V, 0.20 nA (e), −1.8 V, 0.15 nA (f), +2.0 V, 0.35 nA (g), and +2.0 V, 0.3 nA (h). Here, negative and positive tip bias refer to imaging of empty and occupied states, respectively. The size of STM images in (e–h) is 15 × 20 nm^2.

In order to identify the nature of the species I–IV, we simulated the STM patterns of a large number of structural motifs by means of density functional theory (DFT) using the Tersoff–Hamann approach (ESI, Section S1†). The simulated and experimental STM patterns were compared with respect to the position, symmetry, and apparent height of the species I–IV (see ESI, Section S3†). The results are summarized in Fig. 2. For the species I, the best agreement was obtained by locating a single OH^- group on top of a surface Co^{2+} cation and a corresponding H^+ on a nearby oxygen anion. The less favorable configurations are listed in ESI (Section S3).† The coverage of OH^- groups on as-prepared $Co_3O_4(111)$ determined by temperature programmed desorption (TPD) is 9% of a surface Co^{2+} density (see ESI, Section S4†).

With respect to the nature of species II, the most satisfactory interpretation of the dark depression is a void associated with a missing Co^{2+} cation (Fig. 2b). The arguments supporting this assignment are given in the ESI (Section S4).† Most interestingly, the assignment of species III is consistent with a substitution of Co^{2+} cations by Pt atoms (Fig. 2c). We assume that the substituted Co^{2+} cation will be incorporated into Co_3O_4, for example *via* diffusion to a step edge, and its chemical potential is therefore equal to μ_{Co} (see ESI, Section S1.3†). Noteworthy, this structure represents the energetically most favourable configuration with respect to adsorption of single Pt atoms in top, bridge, and FCC sites on $Co_3O_4(111)$ (ESI, Section S5†).

The Bader charge on Pt atom substituting Co^{2+} is $+1.13e$ which corresponds to the oxidation state Pt^{2+} (ESI, Section S5†). Formally, the cation exchange is accompanied by the charge transfer from the Pt atom to Co^{3+} yielding Co^{2+} cations in the sub-surface region. Finally, the appearance of species IV (triangular protrusions at FCC sites) in STM are best represented by simulated patterns of triaqua complexes (Fig. 2d). These complexes result from the dissociation of three water molecules at a Pt atom in the FCC site followed by its decoration with three OH^- groups interacting with three H^+ adsorbed on oxygen anions. In this configuration, Pt becomes octahedrally coordinated and gains a Bader charge $+1.75e$ which corresponds to the oxidation state Pt^{4+} (ESI, Section S5†). For comparison, the dissociation of a single water molecule at the

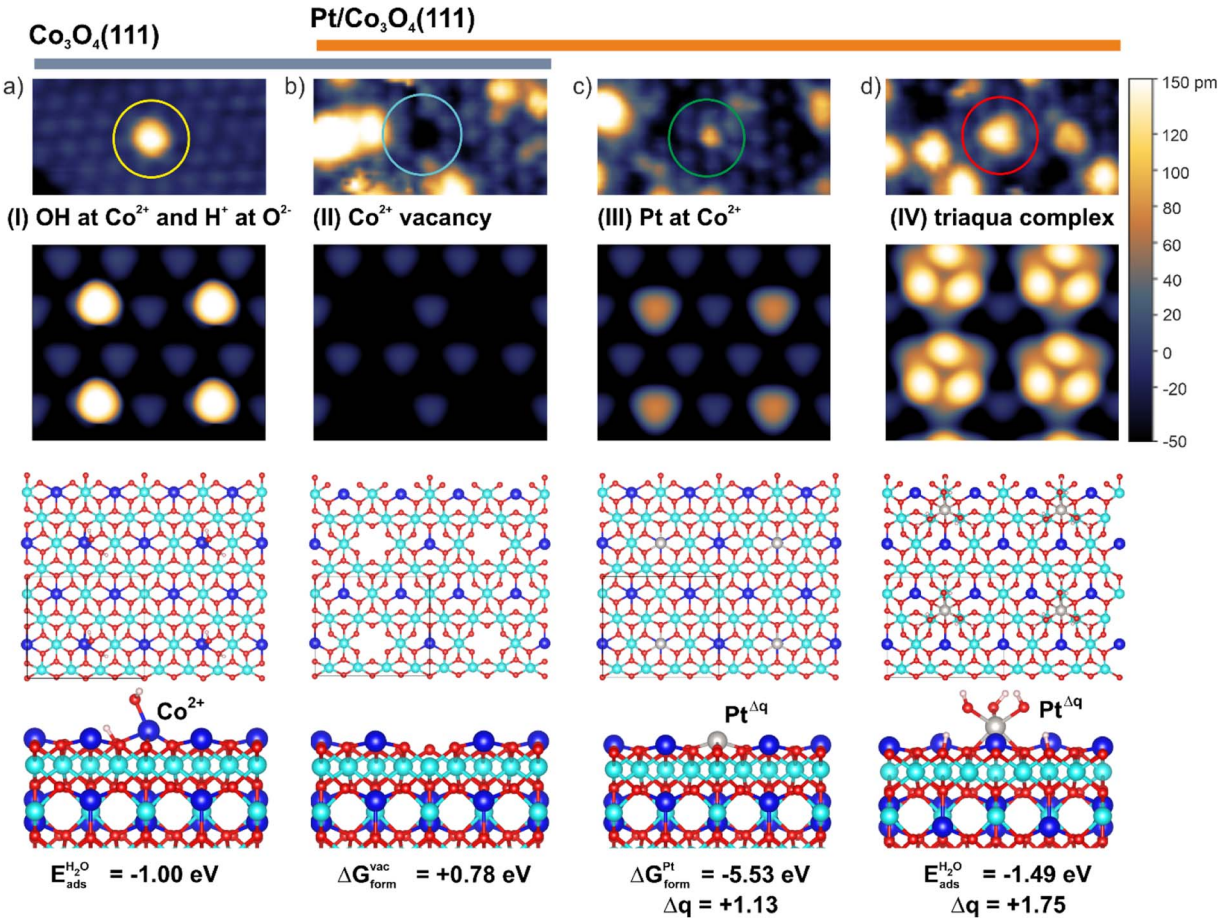

Fig. 2 Assignment of species I–IV: the features in the STM images (top) of $Co_3O_4(111)$ (a) and model $Pt/Co_3O_4(111)$ systems (b–d) are assigned based on simulated STM patterns (middle). The sizes of the STM images are 5×2.5 nm^2 (top) and 2.3×2.0 nm^2 (middle). The STM images in the top and middle panels are plotted on the same apparent height scale. The ball models (bottom) represent the structure and coordination environment of the species (I–IV). The blue and cyan balls represent Co^{2+} and Co^{3+} cations while grey, red, and small white balls represent Pt, oxygen, and hydrogen, respectively. E_{ads} indicates adsorption energies while ΔG_{form} indicate formation free energies. Both quantities are defined in the ESI, Section S1.3.†

Pt atom in the FCC site yields an adsorption energy similar to that calculated for the triaqua complex (ESI, Section S6†). However, the Bader charge on the Pt atom decorated by a single OH^- group at the FCC site merely increases from +0.79*e* to +0.99*e* corresponding to a formal oxidation state of approximately Pt^{2+}. If such species exist, they would contribute to the intensity of the Pt 4f contribution at 72.3 eV (Pt $4f_{7/2}$). The formation of a triaqua complex at Pt^{2+} cations substituting Co^{2+} is less favorable (see ESI, Section S6†). However, we believe that the formation of the triaqua complexes at Pt atoms substituting surface Co^{2+} would lead to their relocation to the more favorable FCC site. This hypothesis is consistent with the increasing number of cationic vacancies (species II).

It is noteworthy, that the species I associated with hydroxyl groups at the surface Co^{2+} cations vanish upon deposition of Pt (see ESI, Table S1†). We found that the adsorption energy of a single dissociated water molecule on the Co^{2+} cation is −1.00 eV, which is lower (*i.e.* less strongly bound) than that calculated for configurations with OH^- groups adsorbed on Pt atoms at the FCC site (−1.51 eV) and Pt^{2+} substituting the surface Co^{2+} cations (−1.24 eV). This observation suggests a strong driving force for a migration of water molecules from Co^{2+} sites in the presence of the Pt atoms.

In order to elucidate the role of water and hydroxyl groups in the atomic dispersion of Pt on $Co_3O_4(111)$, we investigated the interaction of Pt with three different types of $Co_3O_4(111)$ substrates denoted as (i) dehydroxylated, (ii) hydroxylated, and (iii) moist. The dehydroxylated substrate was prepared by a brief annealing of the $Co_3O_4(111)$ film at 650 K in UHV. The hydroxylated and moist substrates were prepared first by a brief annealing of the $Co_3O_4(111)$ film at 650 K in UHV followed by its exposure to 20 L (1 Langmuir (L) = 1.33×10^{-6} mbar × s) of water at 300 K (hydroxylated) and at 100 K followed by brief annealing to 170 K in UHV (moist). The O 1 s spectra obtained from the dehydroxylated, hydroxylated, and moist $Co_3O_4(111)$ surfaces are discussed in ESI (Section S7).† Respectively, we obtained a dehydroxylated substrate, which is virtually free of hydroxyl groups and molecular water, and, hydroxylated and moist substrates containing predominantly hydroxyls and molecular water in the form of mixed OH^-/H_2O clusters.[51] The Pt 4f spectra obtained after the deposition of 0.1 ML Pt onto the dehydroxylated, hydroxylated, and moist $Co_3O_4(111)$ surfaces and subsequent annealing in UHV are shown in Fig. 3a.

Note, that in the case of the moist surface, Pt was deposited at 100 K in order to prevent desorption of molecularly adsorbed water which typically occurs around 200 K.[51] In the Pt 4f spectra obtained from the three samples, we resolved two Pt 4f contributions discussed above. Thus, the main ionic species are Pt^{2+} substituting Co^{2+} cations (Fig. 3b) and triaqua complexes (Fig. 3c). In addition, all samples contain ultra-small $Pt^{\delta+}$ aggregates. We analyzed the structure and the distribution of Bader charge in ultra-small $Pt^{\delta+}$ aggregates as a function of size (Fig. 3d–f and ESI, Section S8†). We found that only those Pt atoms that are in direct contact with the oxide substrate exhibit significant positive charge. The adsorption energy per Pt atom increases with size, suggesting a tendency for Pt atoms to form clusters (Fig. 3d–f).

Surprisingly, the amounts of Pt^{4+} species formed upon Pt deposition on all three surfaces are similar (Fig. 3a) despite pronounced differences in the oxidation state of the $Co_3O_4(111)$

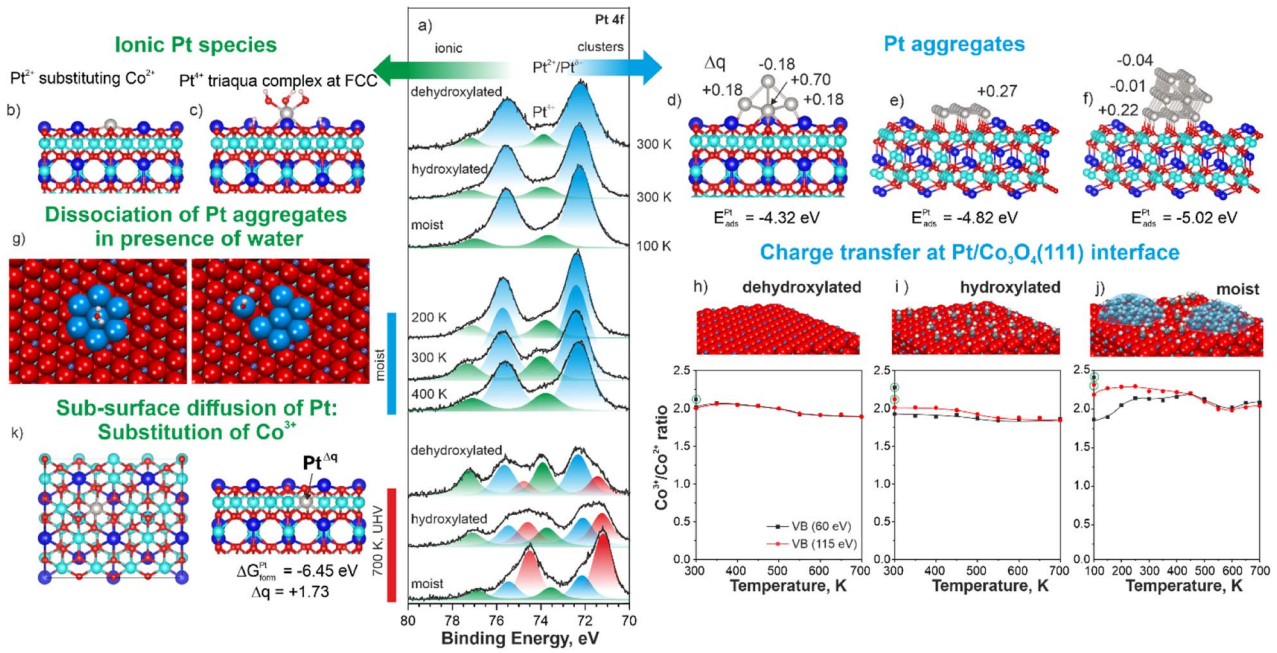

Fig. 3 Role of water: Pt 4f spectra obtained from model Pt/Co_3O_4(111) systems (a) prepared by deposition of 0.10 ML of Pt on (i) dehydroxylated, (ii) hydroxylated, and (iii) moist $Co_3O_4(111)$ surfaces in UHV followed by annealing in UHV. The most abundant ionic species (b and c) and Pt aggregates (d–f). A schematic scenario for dissociation of Pt aggregates in the presence of water (g). Charge transfer at the Pt–$Co_3O_4(111)$ interface monitored as Co^{3+}/Co^{2+} ratio upon annealing of dehydroxylated, hydroxylated, and moist Pt/$Co_3O_4(111)$ systems in UHV (h–j). DFT calculations of subsurface diffusion of Pt atoms by means of substituting Co^{3+} by Pt^{4+} (k).

supports. The corresponding Co^{3+}/Co^{2+} concentration ratios are plotted in Fig. 3h–j. Typically, we quantify the oxidation state of $Co_3O_4(111)$ based on the changes in the Co^{3+}/Co^{2+} concentration ratios obtained by the analysis of the valence band spectra.[52] The Co^{3+}/Co^{2+} concentration ratio was monitored using two different photon energies yielding surface (60 eV) and sub-surface (115 eV) information. Prior to Pt deposition (see circled dots in Fig. 3h–j), the Co^{3+}/Co^{2+} ratios deviate from the stoichiometric ratio; the deviation is the highest on moist substrate suggesting partial oxidation of the surface layer triggered by the reaction with water. The evolution of the Co^{3+}/Co^{2+} ratio upon annealing of Pt-free $Co_3O_4(111)$ exposed to 20 L of water is shown in ESI (Section S10).†

Deposition of Pt results in partial reduction of $Co_3O_4(111)$ substrates due to the EMSI, *i.e.* charge transfer from Pt to Co_3O_4. A more pronounced charge transfer upon Pt deposition on the moist substrate results from the migration of water/hydroxyls from Co^{2+} cations to Pt sites. As predicted by DFT, this process results in an increase of the Bader charges on the Pt sites as a function of the degree of hydroxylation. In the next step, annealing at 350 K leads to an increase of the amount of Pt^{4+} at the expense of the $Pt^{2+}/Pt^{\delta+}$ species on all three samples: the amount of the Pt^{4+} species is significantly higher on the moist surface. This observation suggests a clear preference for the formation of triaqua complexes. We modelled the energetics of the formation of the triaqua complexes also by dissociation of the $Pt^{\delta+}$ aggregates (Fig. 3g). Our study suggests that such scenario is thermodynamically favorable based on the residual partial pressure of water in the analysis chamber (see ESI, Section S9†). Upon further annealing, the Pt^{4+} species are converted to $Pt^{2+}/Pt^{\delta+}$ below 450 K and metallic Pt^0 above 450 K (see ESI, Section S7†). This process is accompanied by re-oxidation of the $Co_3O_4(111)$ substrate mostly due to H_2 desorption, which has been reported previously for different systems under similar conditions.[53] We experimentally verified H_2 desorption from Pt-free $Co_3O_4(111)$ substrate and $Pt/Co_3O_4(111)$ system under relevant conditions (ESI, Section S10†). Surprisingly, annealing above 600 K once again triggers the formation of Pt^{4+} species accompanied by Pt^0 at the expense of the $Pt^{2+}/Pt^{\delta+}$ species. The depth profiling of the Pt^{4+} distribution within the $Pt/Co_3O_4(111)$ system, suggests its sub-surface location (ESI, Section S11†). Our DFT calculations indicate that the most favorable configuration for the Pt^{4+} species corresponds to the substitution of Co^{3+} cations by Pt atoms. This process has a formation free energy of −6.45 eV and leads to an increase of the Bader charge on Pt to +1.73*e* (Fig. 3k). Noteworthy, this process is not accompanied by the reduction of the $Co_3O_4(111)$ support (see Fig. 3h–j). We excluded the formation of metallic Pt–Co alloys (see ESI, Section S12†). Accordingly, the charge transfer must occur exclusively between Pt species (*e.g.* charge disproportionation between two Pt^{2+} species yielding Pt^{4+} and Pt^0).

The role of water is to form triaqua complexes at FCC sites either by stabilizing the deposited Pt atoms at FCC sites or by conversion of Pt^{2+} at substitutional Co^{2+} sites. The latter channel involves relocation of a triaqua complexes to the FCC sites leaving a cationic vacancy behind. This pathway is irreversible, *i.e.* after the loss of hydroxyl groups, Pt species in FCC sites are prone to sintering. As a result, after annealing at 700 K, the amount of Pt^0 is the highest and the amount of Pt^{4+} species is the lowest on the moist substrate and *vice versa* on the dehydroxylated substrate (Fig. 3a).

Conclusions

We have demonstrated that atomically dispersed Pt species can be formed at a high density on a flat surface of a reducible oxide. A key element is the termination of the surface by surface cations, which can be substituted by the noble metal species. Specifically, on the well-ordered $Co_3O_4(111)$ surface, atomically dispersed Pt species are formed in the oxidation states of Pt^{2+} and Pt^{4+}. The mechanism associated with the EMSI involves temperature-controlled substitution of surface Co^{2+} and sub-surface Co^{3+} cations by Pt^{2+} and Pt^{4+} cations, respectively. In the presence of co-adsorbed water, Pt^{4+} species can be stabilized at the surface in the form of triaqua complexes at FCC sites. This pathway potentially lowers the number of surface Pt^{2+} species yielding cationic vacancies. Under these conditions, substitution of sub-surface Co^{3+} by Pt^{4+} cations is suppressed which leads to the formation of metallic Pt^0. This complex mechanism highlights the dynamic nature of the catalyst surface. In this respect, we provide the atomic-level understanding of the EMSI and the specifics of the charge transfer upon the cation exchange which can guide the design of the high-density SAC.

Data availability

Source data are provided at Zenodo[54]: **https://doi.org/10.5281/zenodo.10229984**.

Author contributions

Conceptualization: M. F. C., J. M., S. P., and Y. L.; funding acquisition: J. M. O. B. J. L. P. K. S. investigation: L. F., M. F. C., M. R., M. K., T. S., P. K. S., N. T., S. M., J. Š., T. D., V. U., V. J., Y. L; supervision: M. S., V. J., S. F., O. B., J. L., J. M., S. P., Y. L.; validation: L. F., M. F. C., P. K. S., M. S., V. J., J. M., YL.; writing – original draft: Y. L.; writing – review and editing: L. F., M. F. C., M. R., M. K., T. S., N. T., S. M., M. S., V. J., O. B., J. L., J. M., S. P., Y. L.; all authors have given approval for the final version of the manuscript.

Conflicts of interest

There are no conflicts to declare.

Acknowledgements

The authors acknowledge financial support by the Deutsche Forschungsgemeinschaft (DFG) (project 431733372) and the Czech Science Foundation (project GAČR 20-11688J). This project has received funding from the European Union's Horizon 2020 research and innovation program under grant

agreement no. 101007417 having benefitted from the access provided by CNR-IOM in Trieste within the framework of the NFFA-Europe Pilot Transnational Access Activity, proposals ID865 and ID186. Additional support is acknowledged by the DFG Collaborative Research Centre SFB 1452 – Catalysis at Liquid Interfaces (project 431791331) and project 453560721. The authors acknowledge financial support from ICSC – Centro Nazionale di Ricerca in High Performance Computing, Big Data and Quantum Computing, funded by European Union – NextGenerationEU. P. K. S. and J. Š. thank for the support of the Grant Agency of Charles University (project GAUK 326122). The authors acknowledge the CERIC-ERIC Consortium for the access to experimental facilities and financial support. The authors also acknowledge the support by Czech Ministry of Education, Youth and Sports (project LM2018116 and project QM4ST, reg. no. CZ.02.01.01/00/22_008/0004572). The authors thank Dr Kevin Charles Prince for the support and organizing the beamtime. The authors thank Prof. Dr M. Alexander Schneider for help with interpretation of STM images and IV-LEED.

References

1 M. Li, A. Groß and R. J. Behm, *ACS Catal.*, 2022, **12**, 10065–10079.
2 T. W. van Deelen, C. Hernández Mejía and K. P. de Jong, *Nat. Catal.*, 2019, **2**, 955–970.
3 J. Chen, Y. Zhang, Z. Zhang, D. Hou, F. Bai, Y. Han, C. Zhang, Y. Zhang and J. Hu, *J. Mater. Chem. A*, 2023, **11**, 8540–8572.
4 C. T. Campbell, *Nat. Chem.*, 2012, **4**, 597–598.
5 A. Bruix, J. A. Rodriguez, P. J. Ramírez, S. D. Senanayake, J. Evans, J. B. Park, D. Stacchiola, P. Liu, J. Hrbek and F. Illas, *J. Am. Chem. Soc.*, 2012, **134**, 8968–8974.
6 G. Pacchioni and H.-J. Freund, *Chem. Soc. Rev.*, 2018, **47**, 8474–8502.
7 Y. Lykhach, S. M. Kozlov, T. Skála, A. Tovt, V. Stetsovych, N. Tsud, F. Dvořák, V. Johánek, A. Neitzel, J. Mysliveček, S. Fabris, V. Matolín, K. M. Neyman and J. Libuda, *Nat. Mater.*, 2016, **15**, 284–288.
8 A. K. Datye and H. Guo, *Nat. Commun.*, 2021, **12**, 895.
9 S. Mitchell and J. Pérez-Ramírez, *Nat. Commun.*, 2020, **11**, 4302.
10 Q. Zhang and J. Guan, *Adv. Funct. Mater.*, 2020, **30**, 2000768.
11 W. Li, Z. Guo, J. Yang, Y. Li, X. Sun, H. He, S. Li and J. Zhang, *Electrochem. Energy Rev.*, 2022, **5**, 9.
12 X. Liang, N. Fu, S. Yao, Z. Li and Y. Li, *J. Am. Chem. Soc.*, 2022, **144**, 18155–18174.
13 F. Kraushofer and G. S. Parkinson, *Chem. Rev.*, 2022, **122**, 14911–14939.
14 A. Bruix, Y. Lykhach, I. Matolínová, A. Neitzel, T. Skála, N. Tsud, M. Vorokhta, V. Stetsovych, K. Ševčiková, J. Mysliveček, R. Fiala, M. Václavů, K. C. Prince, S. Bruyere, V. Potin, F. Illas, V. Matolín, J. Libuda and K. M. Neyman, *Angew. Chem., Int. Ed.*, 2014, **53**, 10525–10530.
15 J. Jones, H. Xiong, A. T. DeLaRiva, E. J. Peterson, H. Pham, S. R. Challa, G. Qi, S. Oh, M. H. Wiebenga, X. I. Pereira Hernández, Y. Wang and A. K. Datye, *Science*, 2016, **353**, 150–154.
16 R. Lang, X. Du, Y. Huang, X. Jiang, Q. Zhang, Y. Guo, K. Liu, B. Qiao, A. Wang and T. Zhang, *Chem. Rev.*, 2020, **120**, 11986–12043.
17 N. J. O'Connor, A. S. M. Jonayat, M. J. Janik and T. P. Senftle, *Nat. Catal.*, 2018, **1**, 531–539.
18 B. T. Qiao, A. Q. Wang, X. F. Yang, L. F. Allard, Z. Jiang, Y. T. Cui, J. Y. Liu, J. Li and T. Zhang, *Nat. Chem.*, 2011, **3**, 634–641.
19 J. Geiger and N. López, *J. Phys. Chem. C*, 2022, **126**, 13698–13704.
20 N. Cheng, L. Zhang, K. Doyle-Davis and X. Sun, *Electrochem. Energy Rev.*, 2019, **2**, 539–573.
21 T. Cui, L. Li, C. Ye, X. Li, C. Liu, S. Zhu, W. Chen and D. Wang, *Adv. Funct. Mater.*, 2022, **32**, 2108381.
22 S. Duan, R. Wang and J. Liu, *Nanotechnology*, 2018, **29**, 204002.
23 G. Di Liberto, S. Tosoni, L. A. Cipriano and G. Pacchioni, *Acc. Mater. Res.*, 2022, **3**, 986–995.
24 Y. Ren, Y. Tang, L. Zhang, X. Liu, L. Li, S. Miao, D. Sheng Su, A. Wang, J. Li and T. Zhang, *Nat. Commun.*, 2019, **10**, 4500.
25 M. Farnesi Camellone, F. Dvořák, M. Vorokhta, A. Tovt, I. Khalakhan, V. Johánek, T. Skála, I. Matolínová, S. Fabris and J. Mysliveček, *ACS Catal.*, 2022, **12**, 4859–4871.
26 A. Tovt, L. Bagolini, F. Dvořák, N.-D. Tran, M. Vorokhta, K. Beranová, V. Johánek, M. Farnesi Camellone, T. Skála, I. Matolínová, J. Mysliveček, S. Fabris and V. Matolín, *J. Mater. Chem. A*, 2019, **7**, 13019–13028.
27 H. N. Pham, A. DeLaRiva, E. J. Peterson, R. Alcala, K. Khivantsev, J. Szanyi, X. S. Li, D. Jiang, W. Huang, Y. Sun, P. Tran, Q. Do, C. L. DiMaggio, Y. Wang and A. K. Datye, *ACS Sustainable Chem. Eng.*, 2022, **10**, 7603–7612.
28 J. R. Regalbuto and A. K. Datye, *Nat. Nanotechnol.*, 2022, **17**, 110–111.
29 J. Shan, J. Liao, C. Ye, J. Dong, Y. Zheng and S.-Z. Qiao, *Angew. Chem., Int. Ed.*, 2022, **61**, e202213412.
30 W. Yang, X. Zhao, Y. Wang, R. Wang, W. Yang, Y. Peng and J. Li, *Nano Res.*, 2023, **16**, 219–227.
31 J. Wu, L. Xiong, B. Zhao, M. Liu and L. Huang, *Small Methods*, 2020, **4**, 1900540.
32 Y. Wang, S. Lee, J. Zhou, J. Fu, A. Foucher, E. Stach, L. Ma, N. Marinkovic, S. Ehrlich, W. Zheng and D. G. Vlachos, *Catal. Sci. Technol.*, 2022, **12**, 2920–2928.
33 H. Shin, J. Ko, C. Park, D.-H. Kim, J. Ahn, J.-S. Jang, Y. H. Kim, S.-H. Cho, H. Baik and I.-D. Kim, *Adv. Funct. Mater.*, 2022, **32**, 2110485.
34 X. Yang and G. Wu, *Angew. Chem., Int. Ed.*, 2023, **62**, e202216490.
35 R. Lang, W. Xi, J.-C. Liu, Y.-T. Cui, T. Li, A. F. Lee, F. Chen, Y. Chen, L. Li, L. Li, J. Lin, S. Miao, X. Liu, A.-Q. Wang, X. Wang, J. Luo, B. Qiao, J. Li and T. Zhang, *Nat. Commun.*, 2019, **10**, 234.
36 X. Hai, S. Xi, S. Mitchell, K. Harrath, H. Xu, D. F. Akl, D. Kong, J. Li, Z. Li, T. Sun, H. Yang, Y. Cui, C. Su, X. Zhao, J. Li, J. Pérez-Ramírez and J. Lu, *Nat. Nanotechnol.*, 2022, **17**, 174–181.

37 J. Hulva, M. Meier, R. Bliem, Z. Jakub, F. Kraushofer, M. Schmid, U. Diebold, C. Franchini and G. S. Parkinson, *Science*, 2021, **371**, 375–379.
38 Z. Jiang, X. Feng, J. Deng, C. He, M. Douthwaite, Y. Yu, J. Liu, Z. Hao and Z. Zhao, *Adv. Funct. Mater.*, 2019, **29**, 1902041.
39 Z. Jakub, J. Hulva, M. Meier, R. Bliem, F. Kraushofer, M. Setvin, M. Schmid, U. Diebold, C. Franchini and G. S. Parkinson, *Angew. Chem., Int. Ed.*, 2019, **58**, 13961–13968.
40 E. Bianchetti, D. Perilli and C. Di Valentin, *ACS Catal.*, 2023, **13**, 4811–4823.
41 F. Kraushofer, L. Haager, M. Eder, A. Rafsanjani-Abbasi, Z. Jakub, G. Franceschi, M. Riva, M. Meier, M. Schmid, U. Diebold and G. S. Parkinson, *ACS Energy Lett.*, 2022, **7**, 375–380.
42 L. Puntscher, K. Daninger, M. Schmid, U. Diebold and G. S. Parkinson, *Electrochim. Acta*, 2023, **449**, 142190.
43 M. C. Biesinger, L. W. M. Lau, A. R. Gerson and R. S. C. Smart, *Appl. Surf. Sci.*, 2010, **257**, 887–898.
44 M. C. Biesinger, B. P. Payne, A. P. Grosvenor, L. W. M. Lau, A. R. Gerson and R. S. C. Smart, *Appl. Surf. Sci.*, 2011, **257**, 2717–2730.
45 Y. Lykhach, S. Piccinin, T. Skála, M. Bertram, N. Tsud, O. Brummel, M. Farnesi Camellone, K. Beranová, A. Neitzel, S. Fabris, K. C. Prince, V. Matolín and J. Libuda, *J. Phys. Chem. Lett.*, 2019, **10**, 6129–6136.
46 W. Meyer, K. Biedermann, M. Gubo, L. Hammer and K. Heinz, *J. Phys.: Condens. Matter*, 2008, **20**, 265011.
47 M. Bertram, C. Prössl, M. Ronovský, J. Knöppel, P. Matvija, L. Fusek, T. Skála, N. Tsud, M. Kastenmeier, V. Matolín, K. J. J. Mayrhofer, V. Johánek, J. Mysliveček, S. Cherevko, Y. Lykhach, O. Brummel and J. Libuda, *J. Phys. Chem. Lett.*, 2020, **11**, 8365–8371.
48 NIST X-ray Photoelectron Spectroscopy Database, *NIST Standard Reference Database Number 20*, National Institute of Standards and Technology, Gaithersburg MD, 2000, p. 20899, DOI: **10.18434/T4T88K**.
49 M. G. Mason, *Phys. Rev. B: Condens. Matter Mater. Phys.*, 1983, **27**, 748–762.
50 G. K. Wertheim and S. B. DiCenzo, *Phys. Rev. B: Condens. Matter Mater. Phys.*, 1988, **37**, 844–847.
51 M. Schwarz, F. Faisal, S. Mohr, C. Hohner, K. Werner, T. Xu, T. Skála, N. Tsud, K. C. Prince, V. Matolín, Y. Lykhach and J. Libuda, *J. Phys. Chem. Lett.*, 2018, **9**, 2763–2769.
52 M. Kastenmeier, L. Fusek, F. Mohamed, C. Schuschke, M. Ronovský, T. Skála, M. Farnesi Camellone, N. Tsud, V. Johánek, S. Fabris, J. Libuda, S. Piccinin, Y. Lykhach, J. Mysliveček and O. Brummel, *J. Phys. Chem. C*, 2023, **127**, 6034–6044.
53 Y. Fujimori, W. E. Kaden, M. A. Brown, B. Roldan Cuenya, M. Sterrer and H.-J. Freund, *J. Phys. Chem. C*, 2014, **118**, 17717–17723.
54 Y. Lykhach, J. Mysliveček, J. Libuda, S. Piccinin and M. Farnesi Camellone, Atomistic Picture of Electronic Metal Support Interaction and the Role of Water, *Zenodo*, 2023, DOI: **10.5281/zenodo.10229984**.